

# Reversible MoS<sub>2</sub> Origami with Spatially Resolved and **Reconfigurable Photosensitivity**

Weinan Xu,<sup>†,∇</sup> Tengfei Li,<sup>‡</sup> Zhao Qin,<sup>§,○</sup> Qi Huang,<sup>†</sup> Hui Gao, Hui Gao, Kibum Kang, Jiwoong Park, Markus J. Buehler, Jacob B. Khurgin, and David H. Gracias\*, †,#

Supporting Information

ABSTRACT: Two-dimensional layered materials (2DLMs) have been extensively studied in a variety of planar optoelectronic devices. Three-dimensional (3D) optoelectronic structures offer unique advantages including omnidirectional responses, multipolar detection, and enhanced lightmatter interactions. However, there has been limited success



in transforming monolayer 2DLMs into reconfigurable 3D optoelectronic devices due to challenges in microfabrication and integration of these materials in truly 3D geometries. Here, we report an origami-inspired self-folding approach to reversibly transform monolayer molybdenum disulfide (MoS<sub>2</sub>) into functional 3D optoelectronic devices. We pattern and integrate monolayer MoS<sub>2</sub> and gold (Au) onto differentially photo-cross-linked thin polymer (SU8) films. The devices reversibly self-fold due to swelling gradients in the SU8 films upon solvent exchange. We fabricate a wide variety of optically active 3D MoS<sub>2</sub> microstructures including pyramids, cubes, flowers, dodecahedra, and Miura-oris, and we simulate the self-folding mechanism using a coarse-grained mechanics model. Using finite-difference time-domain (FDTD) simulation and optoelectronic characterization, we demonstrate that the 3D self-folded MoS<sub>2</sub> structures show enhanced light interaction and are capable of angle-resolved photodetection. Importantly, the structures are also reversibly reconfigurable upon solvent exchange with high tunability in the optical detection area. Our approach provides a versatile strategy to reversibly configure 2D materials in 3D optoelectronic devices of broad relevance to flexible and wearable electronics, biosensing, and robotics.

**KEYWORDS:** 2D materials, self-folding, photodetectors, optoelectronics, optics

wo dimensional layered materials (2DLMs) have been extensively studied for electronics, optoelectronics, energy,<sup>3</sup> and sensing applications.<sup>4</sup> Monolayer 2DLMs offer unique properties,<sup>5</sup> including atomic-scale thickness, excellent electrical and thermal characteristics, high stability, and mechanical strength.<sup>6,7</sup> Despite significant progress, most monolayer 2DLM-based functional devices are configured on rigid planar substrates which can limit device functionality and increase overall device size. Because monolayer 2DLMs are extremely thin, they possess low bending rigidity,8 and it has been suggested that they could be curved or folded to create three-dimensional (3D) flexible and reconfigurable devices with small form factors; 9,10 however, achieving this vision is challenging.<sup>11</sup> Most high-quality monolayer 2DLMs are grown on rigid substrates using high-temperature chemical vapor deposition (CVD) approaches not compatible with flexible and stimuli responsive polymeric materials. Also, due to the extremely low bending stiffness and strong van der Waals

interactions between these ultrathin films, it is challenging to achieve well-controlled and reversible folding. 12,13

Three-dimensional structures offer significant advantages for optoelectronic applications as has been demonstrated with conventional semiconductors such as silicon and III-V materials. 14,15 For example, macroscale 3D silicon photovoltaic (PV) structures with integrated absorbers and reflectors or kirigami-patterned gallium arsenide solar cells<sup>17</sup> were shown to generate much higher energy densities as compared to flat PV panels. For photodetection and imaging, 3D deformable silicon photodetector arrays were shown to have nearly infinite depth of field and a full field of view with zero aberration. 18,19

2DLMs have unique advantages over conventional semi-conductors in optoelectronics,  $^{20,21}$  including light absorption

Received: July 29, 2019 Revised: October 19, 2019 Published: October 28, 2019



<sup>&</sup>lt;sup>†</sup>Department of Chemical and Biomolecular Engineering and <sup>‡</sup>Department of Electrical and Computer Engineering, Johns Hopkins University, Baltimore, Maryland 21218, United States

<sup>§</sup>Department of Civil and Environmental Engineering, Massachusetts Institute of Technology, Cambridge, Massachusetts 02139, United States

Department of Chemistry, Institute for Molecular Engineering, and Frank Institute, University of Chicago, Chicago, Illinois 60637, United States

<sup>&</sup>lt;sup>1</sup>Department of Chemistry and Chemical Biology, Cornell University, Ithaca, New York 14850, United States

<sup>&</sup>lt;sup>#</sup>Department of Materials Science and Engineering, Johns Hopkins University, Baltimore, Maryland 21218, United States

over a wide energy spectrum, ultrafast carrier dynamics, tunable optical properties via doping, and low dissipation rates.<sup>22</sup> However, their atomically thin structure is a limitation in optical devices due to low light absorption and limited light-matter interactions. 23,24 Strain engineering or shape transformation of 2DLMs into well-defined 3D structures provides a promising strategy to overcome this limitation. <sup>25–27</sup> One recent report showed that a mechanically assembled 3D device based on 2DLMs was capable of measuring the direction, intensity, and angular divergence properties of the incident light.<sup>28</sup> However, reversible, reconfigurable, and stimuli-responsive 3D optoelectronic devices based on monolayer 2DLMs have yet to be achieved and this is an important step in the development of biomimetic, adaptive, smart, wearable, and robotic devices, <sup>29,30</sup> such as those capable of sun tracking (heliotropism), leaf opening (nyctinasty), or structurally tuning color.31

In this work, we reversibly transform monolayer MoS<sub>2</sub> from a flat state to complex 3D shapes, by attaching it to differentially cross-linked and stimuli responsive polymer (SU8) films with integrated gold (Au) electrodes. We report several important advances as compared to prior research. First, we can control both the folding extent and the direction of MoS<sub>2</sub>-Au-SU8 based on the tunable photo-cross-linking of SU8; this control enables the folding of complex Miura-ori patterns which require bidirectional hinges with rigid segments. Such geometries represent a significant advance beyond simple self-folded and unidirectionally curved structures such as cylinders and rolls.<sup>34</sup> The realization of the Miura fold pattern is also a major step toward realizing more complicated origami/kirigami-inspired and deployable functional devices. Second, our approach enables the arrangement and reconfiguration of MoS<sub>2</sub>-based optoelectronic devices in predesigned 3D patterns, leading to spatially or angle-resolved photodetection and vastly tunable detection area between the flat and folded states. Third, the stimulus responsive folding is completely reversible without the need for tethers or wires, and it also has the advantage of being flexible and soft as compared to inorganic or metallic 3D structures, which paves the way for next-generation adaptive, biomimetic, and environmentally responsive optoelectronic devices. Finally, our 3D fabrication technique is based on SU8, which is a negative photoresist widely used in conventional microfabrication.

The fabrication and self-folding process of the MoS<sub>2</sub>–SU8 structures with integrated Au patterns is shown in Figure 1 and more details are in the SI (Figures S1–S3). Briefly, the process involved MoS2 transfer, multistep photopatterning, and etching. We used monolayer MoS2 film synthesized using metal organic chemical vapor deposition (MOCVD), the details of which can be found in a previous report.<sup>35</sup> The Raman spectrum of the synthesized MoS<sub>2</sub> shows peaks at 386 and 406 cm<sup>-1</sup>, and the photoluminescence spectrum has a pronounced peak at 658 nm (Figure S4), which indicates the high quality of MoS<sub>2</sub> used in this study. <sup>36</sup> We transferred a monolayer of MoS<sub>2</sub> from the growth substrate to the top of a silicon wafer which was coated with a copper or aluminum sacrificial layer. We utilized the poly(methyl methacrylate) (PMMA) transfer method.<sup>37</sup> Then, we deposited and photolithographically patterned Au patterns on the MoS<sub>2</sub> by thermal evaporation and a lift-off process. We subsequently deposited, differentially photo-cross-linked, and patterned the SU8 into the predesigned 2D shape. We then removed the excess MoS<sub>2</sub> using oxygen plasma etching. Finally, we released the MoS2-

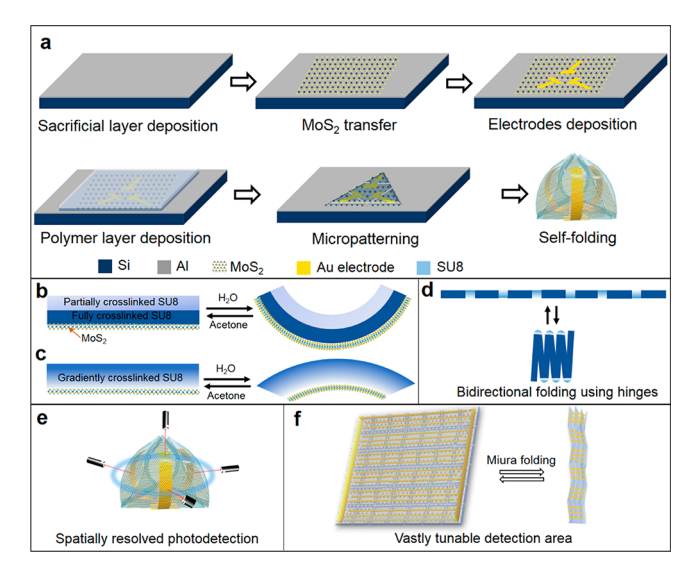
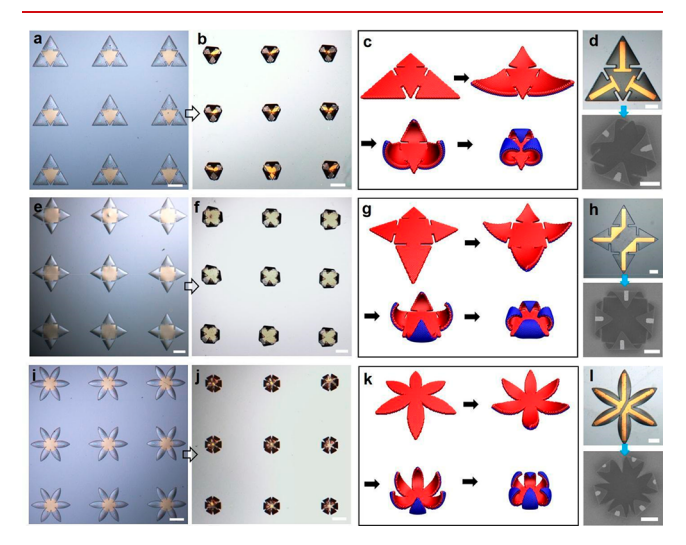


Figure 1. Illustration of the fabrication process for 3D self-folded MoS<sub>2</sub>-Au-SU8 photodetectors. (a) A sacrificial film was deposited on a silicon wafer substrate, followed by transfer of monolayer MoS<sub>2</sub> and photolithographic definition of Au patterns. Then SU8 was patterned by UV irradiation through a photomask. Finally, the MoS<sub>2</sub>-SU8 microstructure was released by dissolving the sacrificial layer and the structures self-folded in water. (b,c) Illustration of the two strategies used to fold the SU8 microstructures. (b) A bilayer SU8 structure with the bottom SU8 layer fully cross-linked, whereas the top SU8 layer partially cross-linked; (c) a thicker SU8 layer with gradient cross-linking density along the thickness. In both cases, reversible self-folding is achieved with solvent exchange. (d) Illustration of bidirectional self-folding of a flat SU8 film into a compact multilayer structure, using two groups of hinges which fold from opposite directions. (e) The 3D MoS<sub>2</sub>-Au-SU8 photodetector is capable of spatially or angle-resolved photodetection. (f) Illustration of a flat MoS<sub>2</sub>-Au-SU8 photodetector with the Miura pattern that can reversibly fold into a compact multilayer structure with significant difference in optical detection area between flat and folded states.

Au-SU8 structures from the silicon or glass substrate by dissolving the sacrificial layer.

Reversible self-folding of the 2D MoS2-SU8 patterned structures is driven by solvent exchange between a good (acetone) and a poor solvent (water) in the differentially photo-cross-linked SU8 films. We utilized two different approaches to achieve the self-folding of the SU8 microstructures, as illustrated in Figure 1b,c. In the first approach, we fabricated an SU8 bilayer with a partially photo-cross-linked top SU8 layer and fully photo-cross-linked the bottom SU8 layer. In the second approach, we created a cross-linking gradient based on the exponential light intensity decay in a single thicker SU8 layer by low UV dose exposure (Figure 1c).<sup>38</sup> Such differentially photo-cross-linked SU8 films could be created with gradients from either top or bottom by light exposure from the top or bottom of the SU8, respectively, and also interspersed with fully cross-linked rigid SU8 panels to create complex designs of bidirectional self-folding structures needed for Miura-ori (Figure 1d). The 3D MoS<sub>2</sub>-SU8 photodetectors assembled by self-folding were characterized by measuring the photovoltage during laser illumination at different angles (Figure 1e). We were also able to assemble reversible Miura-ori inspired photodetectors with a vastly different optical detection area in the flat and folded states (Figure 1f).

The fabrication and assembly process are parallel and can be done in a wafer-scale manner enabling the high-throughput assembly of a wide range of curved and folded 3D-shaped devices from their planar precursors. As shown in Figure 2, a



**Figure 2.** Self-folding of  $MoS_2$ –SU8 structures with different shapes. (a–j) Optical microscope images of the parallel self-folding process of (a,b) pyramid, (e,f) square pyramid, and (i,j) flower-shaped SU8 structures, respectively. The central colored region is due to pinning of the SU8 by selective patterning of the sacrificial layer. (c,g,k) Snapshots of the self-folding process obtained from coarse-grained mechanics simulations for the (c) pyramid, (g) square pyramid, and (k) flower-shaped SU8 structures. (d,h,l) Optical image (top panels) of the patterned  $MoS_2$ –Au–SU8 planar precursors and SEM image (bottom panels) of the assembled  $MoS_2$ –Au–SU8 (d) pyramid, (h) square pyramid, and (l) flower-shaped photodetectors. Scale bars are 500 μm for panels a, b, e, f, i, and j and 200 μm for panels d, h, and l.

pyramid can be generated from its triangular precursor (Figure 2a,b); a square pyramid structure folded from a star-shaped precursor (Figure 2e,f); and a closed flower structure folded from a flat six-petal precursor (Figure 2i,j). It is noteworthy that in these 3D structures, the center SU8 panel are fully cross-linked and pinned on the wafer by the selective patterning of the sacrificial layer to facilitate imaging and characterization. Selective pinning of different regions of the self-folding structure is important to realize on-chip devices. Alternatively, fully freestanding devices can be generated using an unpatterned sacrificial layer.

We note that the self-folding is uniform with a high yield above 95%. The speed of the folding process depends on the thickness and the overall dimensions of the SU8. The structures shown in Figure 2 self-folded within minutes after immersion in water (Figure S5) and reversibly unfolded within 20 s when the solvent was changed to acetone (Figure S6). This folding and unfolding process can be repeated numerous times (>20) without noticeable changes in shape. Also, the high quality of the MoS<sub>2</sub> monolayer is retained before and after the solvent-induced folding/unfolding process (Figure S7). We note that chemically responsive self-folding can enable autonomous operation in biological, ambient, and marine environments and acetone and water are common solvents. However, for some applications solvent exchange-induced folding may be not desirable and in these cases one could replace SU8 with alternate stimuli responsive materials such as temperature or light responsive polymers.

We investigated the mechanics of the self-folding process by developing a coarse-grained model to simulate the shape transformation. The SU8 photoresist is composed of an epoxy base and photoacid generator. The epoxy groups in the resin cross-link upon UV irradiation and subsequent postexposure bake. Depending on the UV exposure dose, the SU8 can be fully cross-linked or partially cross-linked (Figure S8). We simulated the SU8 bilayer with each of the two SU8 layers represented by a coarse-grained membrane with a facecentered cubic (fcc) lattice (a is the lattice constant) to model the location of the mass beads, and elastic springs to model the interaction between the nearest neighboring beads. The thickness (5  $\mu$ m of each layer) as well as the lateral dimension of each layer was set to match the experimental values exactly. In the MoS<sub>2</sub>-SU8 bilayer structures, the bottom SU8 layer was fully cross-linked, whereas the top SU8 layer is partially (about 60%) cross-linked. In the model, the bending stiffness of the fully cross-linked bottom layer  $(D_h)$  is 4.2  $\times$  $10^{-8}~{
m N\cdot m^{39}}$  and that of the partially cross-linked top layer  $(D_{
m t})$ was approximately 60% of  $D_{\rm b}$  and could be varied depending on the cross-linking extent or UV dose (the ratio  $\lambda = D_t/D_b$ ).

When the bilayer is transferred from a good solvent (acetone) to a bad solvent (water), the partially cross-linked porous top layer shrinks in order to minimize its contact with water, and the fully cross-linked bottom layer remains intact. The effect of exposing SU8 to water and the subsequent shrinkage was simulated by decreasing the equilibrium length constant of the fcc lattice in the top layer. Details of the model can be found in the SI.

Snapshots of self-folded structures obtained using the coarse-grained model at different folding stages for pyramid, square pyramid, and flower, are shown in Figure 2c,g,k, respectively. With the shrinkage of the top layer, the panels located around the center start to curve and eventually fold toward the center part. The final stage of the folding corresponds to a mismatch strain  $(1 - a/a_0)$  of 0.15, which corresponds to a surface area shrinkage of 27.8%. We found that the bending stiffness difference between the top and bottom layer also affects the folding, and for a softer top layer the folding extent for a given mismatch strain decreases (Figure S10).

When monolayer MoS<sub>2</sub> and Au patterns are integrated with the differentially photo-cross-linked SU8, a variety of selffolding photodetectors such as pyramid, square pyramid, and flower shapes can be generated (Figure 2d,h,l). We investigated the optoelectronic characteristics of the MoS<sub>2</sub>-Au-SU8 photodetectors by first measuring the photovoltage of the flat precursors. As shown in Figure 3a, we irradiated the flat precursor using a focused laser from the objective of a confocal laser scanning microscope and collected the electrical signals from copper wires bonded to the Au pads (more details in SI). We spatially scanned the laser position along the direction perpendicular to the electrodes (Y-direction) and observed a large photovoltage when the laser was positioned over the MoS<sub>2</sub>-Au regions, reaching a maximum at the first Au electrode and decreasing to zero when the laser spot was in between electrodes, then increasing to another maximum (opposite value) at the second electrode. This periodic pattern of vanishing and maximal photovoltage was repeatedly observed when the laser was moved over the MoS2-Au patterns along the *Y*-direction.

We rationalize this observation by noting that the photovoltage generated is due to the combination of photovoltaic

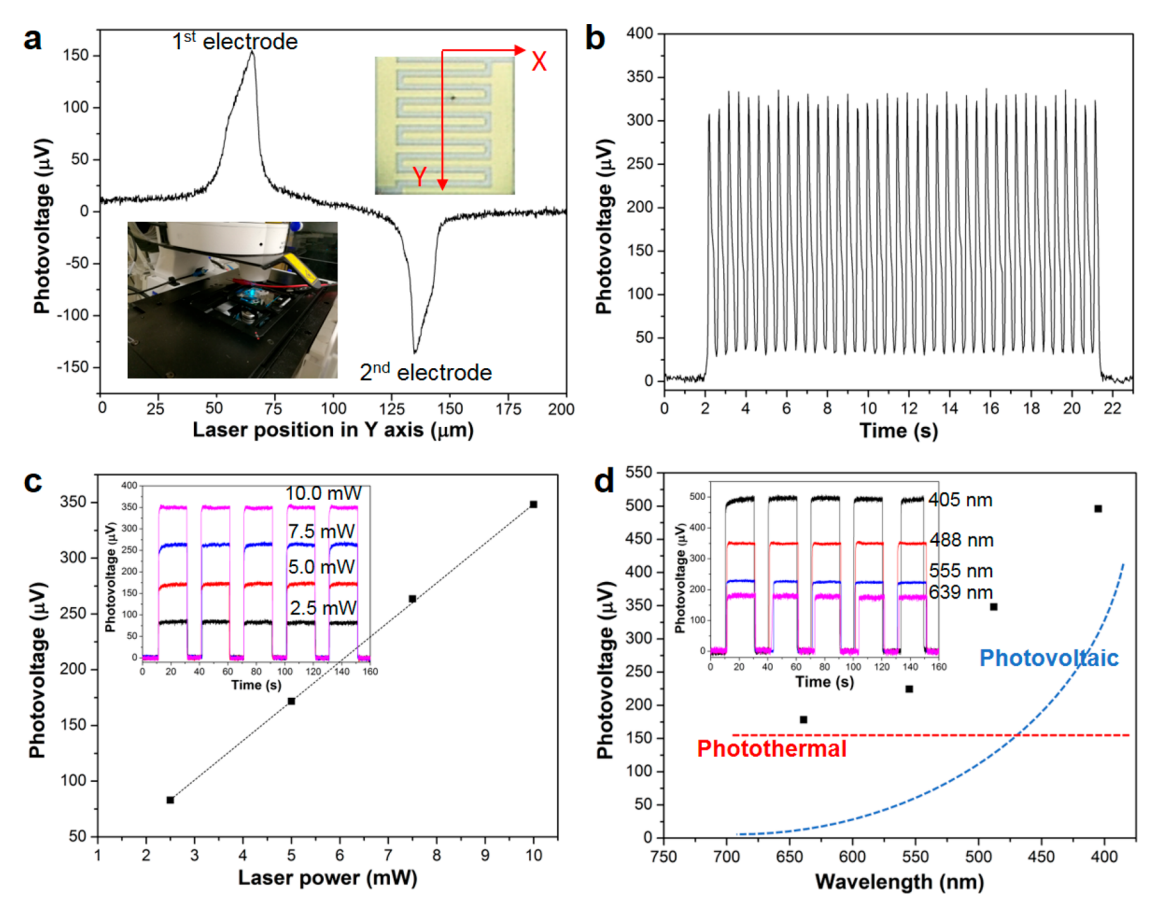


Figure 3. Photoresponse of the MoS<sub>2</sub>-Au-SU8 structures. (a) Plot of the photovoltage as a function of the relative position of the laser spot as it is scanned across the Y-axis of the flat MoS<sub>2</sub>-Au-SU8 photodetector. The insets show optical images of the device (top right), and the experimental setup used for photoresponse measurement (bottom left). (b) Plot of the time-resolved photovoltage when illuminated with a 488 nm laser at 10 mW at intervals of 500 ms (2 Hz). (c) Plot of the photovoltage measured from the MoS<sub>2</sub>-Au-SU8 structure under 488 nm illumination as a function of laser power. (d) Plot of the photovoltage measured from the MoS<sub>2</sub>-Au-SU8 structure under illumination with lasers of different wavelength at a constant power of 10 mW. The dashed lines represent the independence of the photothermal and quadratic functional dependence of the photovoltaic contributions to the photovoltage as a function of wavelength (equations in SI).

(PV) and photothermoelectric (PTE) effects. 40 In principle, both PV and PTE effects are related and associated with the injection of hot carriers across the potential barrier on the MoS<sub>2</sub>-Au interface. When photons get absorbed in the metal and its junction with MoS2, electron-hole pairs are excited. When one of the carriers (usually the electron) get injected into the MoS2 and then diffuses in the lateral direction, a photovoltage is generated. On the other hand, when the photoexcited hot electron shares its energy with other electrons following rapid electron-electron scattering processes, these hot carriers undergo thermal diffusion leading to the establishment of photothermal voltage. 40 In addition to the photovoltaic response, the detector can also be operated under bias, that is, in a photoconductive mode. The I-V curves measured from the MoS2-Au patterns are linear and symmetric for all the bias voltages, indicating an ohmic-like contact, and the current increases as the device is illuminated (Figure S11). The current also increases with bias voltage due to the increase in carrier drift velocity and related reduction of the carrier transit time.<sup>2</sup>

We studied the photoresponse dynamics of the MoS<sub>2</sub>-Au patterns by measuring the rise and fall time under illumination of a modulated light source that could be switched on and off. We utilized a modulated laser with wavelength of 488 nm and 2 Hz frequency for those experiments. The steep rise and fall

edges suggest a reasonably fast response speed (Figure 3b). We characterized the speed of the photodetector by calculating the rise time ( $T_r$ , the time interval from 10% to 90% of the maximum photovoltage) and the fall time ( $T_\theta$  the time interval from 90% to 10% of the maximum photovoltage) of its response to an impulse light signal. The MoS<sub>2</sub>–Au–SU8 photodetector shows a  $T_r$  of 60 ms, and a  $T_f$  of 86 ms. The photoresponse speed is lower than that of similar devices fabricated on rigid substrates such as SiO<sub>2</sub> due to the large number of surface traps and the rough SU8 surface. The response speed can be further increased by encapsulating the MoS<sub>2</sub> with a high-K dielectric layer such as  $Al_2O_3$ .

To study the dependence of the photovoltage on laser power, we varied the 488 nm laser power from 2.5 to 10.0 mW, and the results are shown in Figure 3c. It can be seen that the photovoltage has a linear dependence on the laser power, and the average value increases from 83  $\mu$ V at 2.5 mW to 348  $\mu$ V at 10.0 mW. Increasing illumination levels results in enhanced photovoltage and photocurrent (Figure S12) due to electronhole pair generation by the light absorption in the Au and MoS<sub>2</sub>. We observed that the photovoltage generated is broad in the visible spectral range, and also dependent on the laser wavelength. As shown in Figure 3d in which lasers with four different wavelengths (405, 488, 555, and 639 nm) with the same laser power (10 mW) are used, the generated

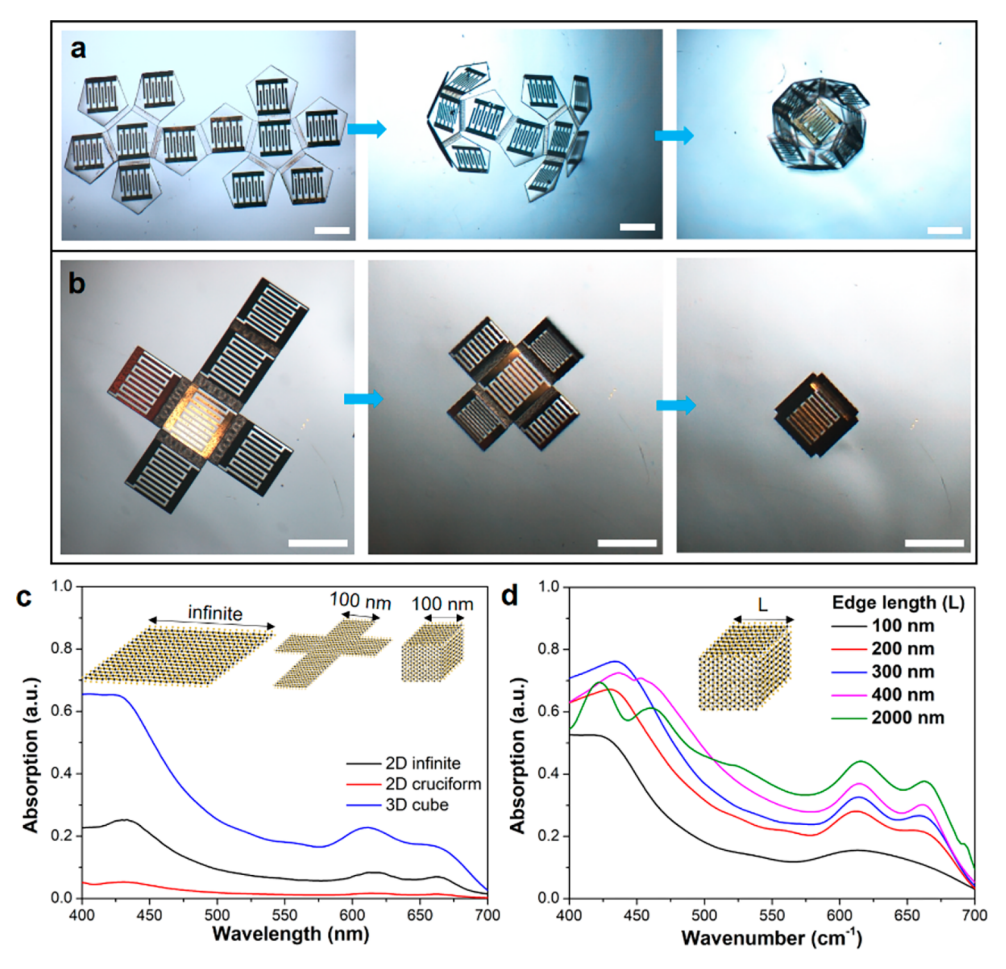


Figure 4. Hinged 3D  $MoS_2$ -Au-SU8 photodetectors with interdigitated electrodes and FDTD simulations of 2D and 3D  $MoS_2$ . (a,b) Self-folding process of, (a) a hinged dodecahedron, and (b) a hinged cube-shaped  $MoS_2$ -Au-SU8 photodetector from their 2D precursors. Scale bars are 1 mm. (c) FDTD simulated absorption spectra of 2D  $MoS_2$  with infinite size, 2D cruciform  $MoS_2$ , and 3D cubic  $MoS_2$ . (d) FDTD-simulated optical absorption spectra of arrays of  $MoS_2$  cubes with different edge lengths.

photovoltage is highest at 405 nm and lowest at 639 nm. As shown by the theoretical curves for PV and PTE indicated by dashed lines, the wavelength dependence can indeed be interpreted as the sum of two effects, a relatively weak PTE voltage and a stronger PV response with the threshold around 650 nm corresponding to the barrier height of about 1.9 eV. 42

Apart from the hingeless self-folding shapes shown in Figure 2, more complicated self-folding requires the incorporation of hinges interspersed by rigid panels. Also, in order to use the MoS2-Au-SU8 photodetectors for spatially resolved photodetection, multiple MoS2-Au patterns need to be defined. Both features are illustrated in the self-folded cubic and dodecahedron MoS2-Au-SU8 photodetectors with interdigitated electrodes on each individual face (Figure 4a,b). In order to study the effect of 3D geometry on the optical properties of MoS<sub>2</sub>, we performed the finite-difference time-domain (FDTD) simulation on flat and cubic MoS<sub>2</sub> nanostructures (Figure 4c, more details in SI). The absorption of a 2D monolayer MoS2 with infinite size was first calculated, and the result agrees well with previous reports. 43,44 Next, we simulated the optical absorption of an array of 3D MoS2 cubes and 2D cruciform MoS2 precursors with the same edge length of 100 nm. We observed that the 2D cruciform MoS2 array has reduced optical absorption due to the reduced interaction area with the electromagnetic field. Importantly, after folding into a cubic shape the optical absorption is significantly enhanced as

compared to the planar  $MoS_2$  with three major broad bands at around 434, 614, and 662 nm.

There are several reasons for this enhanced optical absorption. First, the electromagnetic wave interacts with multiple layers of MoS<sub>2</sub> in the cube as compared to a single planar layer for the 2D MoS<sub>2</sub>. Second, we observed strong coupling of the electric field at the boundaries and corners of MoS<sub>2</sub> cubes (Figure S17), which also leads to stronger energy absorption. We also found that the size and spacing of the MoS<sub>2</sub> cubes have strong effects on their optical properties. Essentially, when the edge length of the cubes increases from 100 to 2000 nm (Figure 4d), the optical absorption gradually increases, except for the decrease in absorption in the 400-500 nm range for the 2000 nm cubes. We rationalize this decrease by noting the edge length of the MoS<sub>2</sub> cubes increases to above the incident light wavelength, and there is strong Fabry-Perot resonance between the top and bottom faces of the MoS<sub>2</sub> cubes which leads to stronger reflection and weaker absorption (Figure S18). This phenomenon is more pronounced at the 400-500 nm range where the conductivity of MoS<sub>2</sub> is high.

Also, for  $MoS_2$  cubes with the same size, the optical absorption is stronger when the spacing between the cubes gets smaller (for instance, from 400 to 25 nm, as shown in Figure S19). The main reason is that with increasing cube size or decreasing spacing between the cubes, the fill ratio is increased, the electric field coupling at the boundaries is also

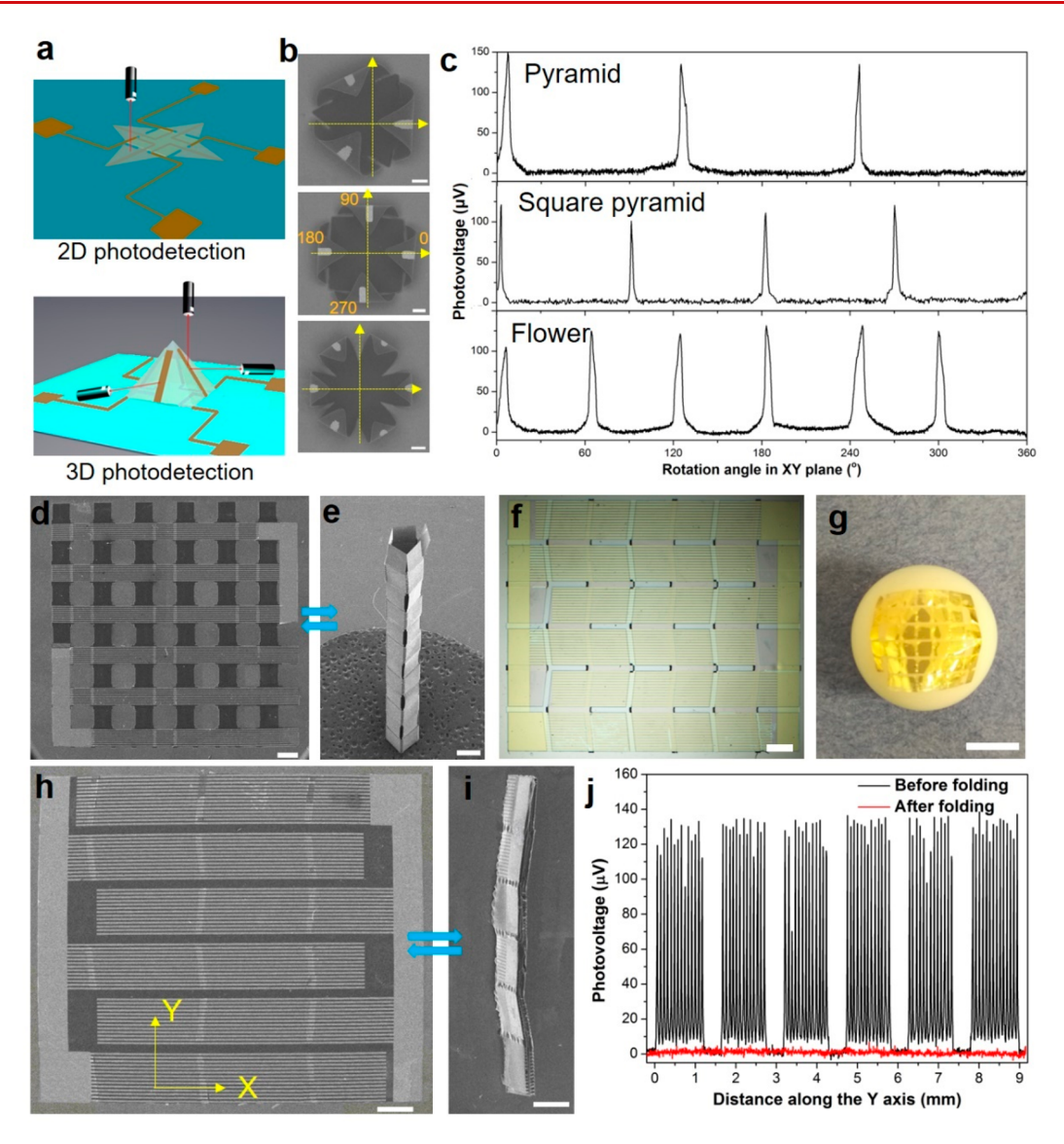


Figure 5. Spatially resolved and reconfigurable photoresponse of self-folded 3D MoS<sub>2</sub>–Au–SU8. (a) Schematic illustration of angle-resolved photodetection capability of the self-folded square pyramid shaped MoS<sub>2</sub>–Au–SU8 photodetector as compared to its 2D counterpart. (b,c) SEM images and angular-dependent photovoltage response of the self-folded pyramid, square pyramid, and flower-shaped 3D MoS<sub>2</sub>–SU8 photodetectors. (d,e) Self-folding transformation of a flat MoS<sub>2</sub>–Au–SU8 photodetector into a compact tower with vastly different spatial arrangement of its functional components. (f) Optical microscope image of a rectangular MoS<sub>2</sub>–Au–SU8 photodetector with Miura-ori pattern consisting of rigid panels and bidirectionally folding hinges. (g) Conformal wrapping of the flexible MoS<sub>2</sub>–Au–SU8 photodetector on a sphere. (h,i) Reversible Miura folding of the 2D MoS<sub>2</sub>–Au–SU8 photodetector from flat to a compact multilayered geometry with vastly different spatial arrangement and significantly reduced detection area in the XY plane. (j) The photovoltage measured from the rectangle MoS<sub>2</sub>–Au–SU8 photodetector before (black line) and after (red line) Miura folding, when the laser is scanned along the Y-axis. All scale bars are 1 mm.

enhanced, and both contribute to the higher energy absorption. The FDTD simulations suggest that such origami-inspired approaches could be used across length scales, and future experiments using electron-beam patterning at sub-100 nm line widths would further augment the present study.

The 3D MoS<sub>2</sub>-Au-SU8 photodetectors also enable spatial and angle-resolved photodetection in all three dimensions. In comparison with conventional 2D photodetectors, which only collect light at limited incident angles (Figure 5a), a 3D photodetector can have multiple electrodes arranged in a 3D fashion and collect light at a wider range of incident angles. In fact, there are major efforts to create 3D optical imagers inspired by the human eye for angular and efficient light

detection and imaging.<sup>18,19</sup> We performed photovoltage measurements using three different shapes of 3D MoS<sub>2</sub>–Au–SU8 photodetector (Figure 5b), with the laser beam (488 nm) irradiated in parallel to the basal plane. Additional details of the experimental setup can be found in the SI (Figure S3). For all the MoS<sub>2</sub>–Au–SU8 structures, multiple equally spaced electrodes were placed, one at each folded panel so that photovoltage would be generated only when the laser beam was incident at those angles or locations (Figure 5c). We chose one of the electrodes as the reference position (zero degree to the center), then successively measured the photovoltage between the reference electrode and all the other electrodes in a counterclockwise manner, while recording the rotating angle of the device in reference to the incident light. For the

pyramid-shaped MoS<sub>2</sub>–Au–SU8, the angle-resolved photovoltage was detected at 0°, 120°, and 240°. Similarly, for the square pyramid MoS<sub>2</sub>–Au–SU8, the angle-resolved photovoltage was detected at 0°, 90°, 180°, and 270°. For the sixpetal flower-shaped MoS<sub>2</sub>–Au–SU8, the angle-resolved photovoltage was detected at 0°, 60°, 120°, 180°, 240°, and 300°. We note that the bending which occurs during self-folding can induce some elastic strain in the MoS<sub>2</sub>, which can lead to band gap modulation 45,46° with associated changes in the photoresponse of the 3D MoS<sub>2</sub>–Au–SU8 at specific wavelengths as compared to its 2D counterpart (Figure S13).

The self-folding of complex 3D structures that show stimuli responsive reversible folding and unfolding with vastly different optical detection areas is a significant advance in this work. In order to illustrate this concept, we reversibly reconfigured a 2D flat MoS2-Au-SU8 photodetector that changes shape into a 3D tower structure with unidirectional folding (Figure 5d,e). Importantly, inspired by the Miura-ori, 48 we were able to create a rectangular-shaped MoS<sub>2</sub>-Au-SU8 photodetector sheet with arrays of Au patterns in the horizontal direction (Figure 5f). The photodetector is highly flexible and can conform to curved objects such as a sphere in analogy to the properties of contact lenses (Figure 5g). The SU8 film is photopatterned such that it contains rigid panels and two types of folding hinges: one group folds upward while the other one folds downward. As a result, the flat rectangular MoS2-Au-SU8 photodetector can be transformed into a compact multilayer-folded shape with a dramatic reduction in light detection area, as shown in the SEM images (Figure 5h,i).

We measured the photovoltage from the Miura photodetector before and after folding (Figure 5j), during which the laser was scanned along the Y-axis of the photodetector. Prior to folding, strong PV is generated when the laser illuminates the MoS2-Au regions as expected. After folding, the Miura pattern folds into an ultracompact multilayer. Interestingly, the folding conceals the MoS2-Au regions within the compact structure and the PV essentially vanishes. After unfolding in acetone, the PV is essentially recovered (Figure S14). This experiment highlights the dramatic tunability that can be achieved in reconfigurable and reversible MoS2-Au-SU8 photodetectors which is an important step toward realizing deployable and smart biomimetic optoelectronic devices. We note that as compared to other designs used in the paper, due to the large strain generated during the Miura folding and unfolding, a fraction of the electrodes was damaged or delaminated after multiple cycles of folding/unfolding (Figure

In summary, we have demonstrated a general approach to reversibly fold high-quality monolayer MoS2 into well-defined 3D structures and optoelectronic devices. Reversible selffolding is based on solvent-induced swelling and deswelling of a differentially photo-cross-linked polymer SU8. The energy for shape transformation is derived from the flow of the solvent in and out of the polymer and does not require any wires, tethers, or batteries. Differential photo-cross-linking enables bending with both positive, zero, and negative curvatures; consequently, we were able to realize both hingeless and bidirectionally hinged 3D structures. We demonstrated that a 3D photodetector based on the folded MoS<sub>2</sub>-Au-SU8 structure offers spatially resolved 3D photodetection capability, which is also tunable depending on the 3D distribution of the MoS<sub>2</sub>-Au patterns. As compared to conventional flat 2D structures, simulations show that 3D MoS<sub>2</sub> structures such as

nanometer-sized cubes offer significantly enhanced light-matter interaction, and strong coupling of electric field at the boundaries and corners. Furthermore, a dramatic reduction and recovery of the MoS<sub>2</sub>—Au—SU8 photodetection area can be achieved with a Miura-ori, which is an advantageous attribute for wearables, as well as portable, foldable, and smart, sensors and energy harvesting devices. We anticipate that this self-folding approach could also be used with other 2D materials. Also, its reliance on planar lithographically patterned precursors and SU8 photoresist suggests the possibility for facile integration with microelectromechanical systems, microfluidics, and complementary metal—oxide—semiconductor to realize even more complex origami-inspired 3D integrated and multifunctional devices.

# ASSOCIATED CONTENT

# Supporting Information

The Supporting Information is available free of charge on the ACS Publications website at DOI: 10.1021/acs.nanolett.9b03107.

Materials and methods, Raman and photoluminescence spectra of MoS<sub>2</sub>; dynamics of the folding and unfolding processes, SEM of the fully and partially cross-linked microstructure of SU8, coarse-grained modeling of the self-folding SU8 bilayer, discussion of the optical response of MoS<sub>2</sub>—Au—SU8 photodetectors, and FDTD simulations of the optical properties of MoS<sub>2</sub> in 2D and 3D geometries (PDF)

# AUTHOR INFORMATION

# **Corresponding Author**

\*E-mail: dgracias@jhu.edu.

#### ORCID ®

Weinan Xu: 0000-0002-5352-3302 Tengfei Li: 0000-0003-0583-8673 Zhao Qin: 0000-0001-5696-8553 Qi Huang: 0000-0002-5524-514X Hui Gao: 0000-0001-8105-2993

Markus J. Buehler: 0000-0002-4173-9659 David H. Gracias: 0000-0003-2735-4725

# **Present Addresses**

V(W.X.) Department of Polymer Engineering, University of Akron, Akron, OH, 44325, U.S.A.

<sup>O</sup>(Z.Q.) Department of Civil and Environmental Engineering, Syracuse University, Syracuse, NY 13244, U.S.A.

(K.K.) Department of Materials Science and Engineering, Korea Advanced Institute of Science and Technology (KAIST), Daejeon 34141, Korea.

#### Notes

The authors declare no competing financial interest.

# ACKNOWLEDGMENTS

We acknowledge funding from the Air Force Office of Scientific Research (AFOSR) MURI program (FA9550-16-1-0031, FA9550-15-1-0514), the National Science Foundation (NSF) (CMMI-1635443 and DMR-1507749). H.G., K.K., and J.P. were also supported by the AFOSR (FA9550-16-1-0347) and the NSF through the Cornell Center for Materials Research with funding from the NSF Materials Research Science and Engineering Centers (MRSEC) program (DMR-1719875) and the University of Chicago MRSEC (NSF DMR-

1420709). M.J.B. and Z.Q. acknowledge support from the Army Research Office, Grant # W911NF1920098.

# REFERENCES

- (1) Fiori, G.; Bonaccorso, F.; Iannaccone, G.; Palacios, T.; Neumaier, D.; Seabaugh, A.; Banerjee, S. K.; Colombo, L. Electronics Based on Two-Dimensional Materials. *Nat. Nanotechnol.* **2014**, *9*, 768–779.
- (2) Lopez-Sanchez, O.; Lembke, D.; Kayci, M.; Radenovic, A.; Kis, A. Ultrasensitive Photodetectors Based on Monolayer MoS2. *Nat. Nanotechnol.* **2013**, *8*, 497–501.
- (3) Anasori, B.; Lukatskaya, M. R.; Gogotsi, Y. 2D Metal Carbides and Nitrides (Mxenes) for Energy Storage. *Nat. Rev. Mater.* **2017**, *2*, 16098.
- (4) Anichini, C.; Czepa, W.; Pakulski, D.; Aliprandi, A.; Ciesielski, A.; Samorì, P. Chemical Sensing with 2D Materials. *Chem. Soc. Rev.* **2018**, 47, 4860–4908.
- (5) Xie, S.; Tu, L.; Han, Y.; Huang, L.; Kang, K.; Lao, K. U.; Poddar, P.; Park, C.; Muller, D. A.; DiStasio, R. A., Jr.; Park, J. Coherent, Atomically Thin Transition-Metal Dichalcogenide Superlattices with Engineered Strain. *Science* **2018**, *359*, 1131–1136.
- (6) Novoselov, K. S.; Fal'ko, V. I.; Colombo, L.; Gellert, P. R.; Schwab, M. G.; Kim, K. A Roadmap for Graphene. *Nature* **2012**, 490, 192–200.
- (7) Novoselov, K. S.; Mishchenko, A.; Carvalho, A.; Castro Neto, A. H. 2D Materials and van der Waals Heterostructures. *Science* **2016**, 353, aac9439.
- (8) Blees, M. K.; Barnard, A. W.; Rose, P. A.; Roberts, S. P.; McGill, K. L.; Huang, P. Y.; Ruyack, A. R.; Kevek, J. W.; Kobrin, B.; Muller, D. A.; McEuen, P. L. Graphene Kirigami. *Nature* **2015**, *524*, 204–207.
- (9) Xu, W.; Gracias, D. H. Soft Three-Dimensional Robots with Hard Two-Dimensional Materials. ACS Nano 2019, 13, 4883–4892.
- (10) Xu, W.; Kwok, K. S.; Gracias, D. H. Ultrathin Shape Change Smart Materials. Acc. Chem. Res. 2018, 51, 436–444.
- (11) Xu, W.; Qin, Z.; Chen, C.; Kwag, H. R.; Ma, Q.; Sarkar, A.; Buehler, M. J.; Gracias, D. H. Ultrathin Thermoresponsive Self-Folding 3D Graphene. *Sci. Adv.* **2017**, *3*, No. e1701084.
- (12) Xu, W.; Paidi, S. K.; Qin, Z.; Huang, Q.; Pagaduan, P. V.; Buehler, M. J.; Barman, I.; Gracias, D. H. Self-Folding Hybrid Graphene Skin for 3D Biosensing. *Nano Lett.* **2019**, *19*, 1409–1417.
- (13) Shenoy, V. B.; Gracias, D. H. Self-Folding Thin-Film Materials: from Nanopolyhedra to Graphene Origami. *MRS Bull.* **2012**, *37*, 847–854.
- (14) Wang, H.; Zhen, H.; Li, S.; Jing, Y.; Huang, G.; Mei, Y.; Lu, W. Self-Rolling and Light-Trapping in Flexible Quantum Well-Embedded Nanomembranes for Wide-Angle Infrared Photodetectors. *Sci. Adv.* **2016**, *2*, No. e1600027.
- (15) Rogers, J.; Huang, Y.; Schmidt, O. G.; Gracias, D. H. Origami MEMS and NEMS. *MRS Bull.* **2016**, *41*, 123–129.
- (16) Bernardi, M.; Ferralis, N.; Wan, J. H.; Villalon, R.; Grossman, J. C. Solar Energy Generation in Three Dimensions. *Energy Environ. Sci.* **2012**, *5*, 6880–6884.
- (17) Lamoureux, A.; Lee, K.; Shlian, M.; Forrest, S. R.; Shtein, M. Dynamic Kirigami Structures for Integrated Solar Tracking. *Nat. Commun.* **2015**, *6*, 8092.
- (18) Song, Y. M.; Xie, Y.; Malyarchuk, V.; Xiao, J.; Jung, I.; Choi, K. J.; Liu, Z.; Park, H.; Lu, C.; Kim, R. H.; Li, R.; Crozier, K. B.; Huang, Y.; Rogers, J. A. Digital Cameras with Designs Inspired by the Arthropod Eye. *Nature* **2013**, *497*, 95–99.
- (19) Zhang, K.; Jung, Y. H.; Mikael, S.; Seo, J. H.; Kim, M.; Mi, H.; Zhou, H.; Xia, Z.; Zhou, W.; Gong, S.; Ma, Z. Origami Silicon Optoelectronics for Hemispherical Electronic Eye Systems. *Nat. Commun.* **2017**, *8*, 1782.
- (20) Xia, F.; Wang, H.; Xiao, D.; Dubey, M.; Ramasubramaniam, A. Two-Dimensional Material Nanophotonics. *Nat. Photonics* **2014**, *8*, 899–907
- (21) Mak, K. F.; McGill, K. L.; Park, J.; McEuen, P. L. The Valley Hall Effect in MoS<sub>2</sub> Transistors. *Science* **2014**, 344, 1489–1492.

- (22) Koppens, F. H. L.; Mueller, T.; Avouris, P.; Ferrari, A. C.; Vitiello, M. S.; Polini, M. Photodetectors Based on Graphene, Other Two-Dimensional Materials and Hybrid Systems. *Nat. Nanotechnol.* **2014**, *9*, 780–793.
- (23) Mueller, T.; Xia, F.; Avouris, P. Graphene Photodetectors for High-Speed Optical Communications. *Nat. Photonics* **2010**, *4*, 297–301.
- (24) Gabor, N. M.; Song, J. C.; Ma, Q.; Nair, N. L.; Taychatanapat, T.; Watanabe, K.; Taniguchi, T.; Levitov, L. S.; Jarillo-Herrero, P. Hot Carrier-Assisted Intrinsic Photoresponse in Graphene. *Science* **2011**, 334, 648–652.
- (25) Wang, L.; Tian, Z.; Zhang, B.; Xu, B.; Wang, T.; Wang, Y.; Li, S.; Di, Z.; Mei, Y. On-Chip Rolling Design for Controllable Strain Engineering and Enhanced Photon-Phonon Interaction in Graphene. *Small* **2019**, *15*, 1805477.
- (26) Kang, P.; Wang, M. C.; Knapp, P. M.; Nam, S. Crumpled Graphene Photodetector with Enhanced, Strain-Tunable, and Wavelength-Selective Photoresponsivity. *Adv. Mater.* **2016**, *28*, 4639–4645.
- (27) Deng, T.; Zhang, Z.; Liu, Y.; Wang, Y.; Su, F.; Li, S.; Zhang, Y.; Li, H.; Chen, H.; Zhao, Z.; Li, Y.; Liu, Z. Three-Dimensional Graphene Field-Effect Transistors as High-Performance Photodetectors. *Nano Lett.* **2019**, *19*, 1494–1503.
- (28) Lee, W.; Liu, Y.; Lee, Y.; Sharma, B. K.; Shinde, S. M.; Kim, S. D.; Nan, K.; Yan, Z.; Han, M.; Huang, Y.; Zhang, Y.; Ahn, J. H.; Rogers, J. A. Two-Dimensional Materials in Functional Three-Dimensional Architectures with Applications in Photodetection and Imaging. *Nat. Commun.* **2018**, *9*, 1417.
- (29) Miskin, M. Z.; Dorsey, K. J.; Bircan, B.; Han, Y.; Muller, D. A.; McEuen, P. L.; Cohen, I. Graphene-Based Bimorphs for Micron-Sized, Autonomous Origami Machines. *Proc. Natl. Acad. Sci. U. S. A.* **2018**, *115*, 466–470.
- (30) Reynolds, M.; McGill, K.; Wang, M.; Gao, H.; Mujid, F.; Kang, K.; Park, J.; Miskin, M.; Cohen, I.; McEuen, P. L. Capillary Origami with Atomically Thin Membranes. *Nano Lett.* **2019**, *19*, 6221–6226.
- (31) Baytekin, B.; Cezan, S. D.; Baytekin, H. T.; Grzybowski, B. A. Artificial Heliotropism and Nyctinasty Based on Optomechanical Feedback and No Electronics. *Soft Rob.* **2018**, *5*, 93–98.
- (32) Li, C.; Liu, Y.; Huang, X.; Jiang, H. Direct Sun-Driven Artificial Heliotropism for Solar Energy Harvesting Based on a Photo-Thermomechanical Liquid-Crystal Elastomer Nanocomposite. *Adv. Funct. Mater.* **2012**, 22, 5166–5174.
- (33) Shang, L.; Zhang, W.; Xu, K.; Zhao, Y. Bio-Inspired Intelligent Structural Color Materials. *Mater. Horiz.* **2019**, *6*, 945–958.
- (34) Deng, T.; Yoon, C.; Jin, Q.; Li, M.; Liu, Z.; Gracias, D. H. Self-folding graphene-polymer bilayers. *Appl. Phys. Lett.* **2015**, *106*, 203108.
- (35) Kang, K.; Xie, S.; Huang, L.; Han, Y.; Huang, P. Y.; Mak, K. F.; Kim, C. J.; Muller, D.; Park, J. High-Mobility Three-Atom-Thick Semiconducting Films with Wafer-Scale Homogeneity. *Nature* **2015**, 520, 656–660.
- (36) De Fazio, D.; Goykhman, I.; Yoon, D.; Bruna, M.; Eiden, A.; Milana, S.; Sassi, U.; Barbone, M.; Dumcenco, D.; Marinov, K.; Kis, A.; Ferrari, A. C. High Responsivity, Large-Area Graphene/MoS<sub>2</sub> Flexible Photodetectors. *ACS Nano* **2016**, *10*, 8252–8262.
- (37) Guimarães, M. H.; Gao, H.; Han, Y.; Kang, K.; Xie, S.; Kim, C. J.; Muller, D. A.; Ralph, D. C.; Park, J. Atomically Thin Ohmic Edge Contacts Between Two-Dimensional Materials. *ACS Nano* **2016**, *10*, 6392–6399.
- (38) Jamal, M.; Zarafshar, A. M.; Gracias, D. H. Differentially Photo-Crosslinked Polymers Enable Self-Assembling Microfluidics. *Nat. Commun.* **2011**, *2*, 527.
- (39) Yu, H.; Balogun, O.; Li, B.; Murray, T. W.; Zhang, X. Building Embedded Microchannels Using a Single Layered SU-8, and Determining Young's Modulus Using a Laser Acoustic Technique. *J. Micromech. Microeng.* **2004**, *14*, 1576–1584.
- (40) Freitag, M.; Low, T.; Xia, F.; Avouris, P. Photoconductivity of Biased Graphene. *Nat. Photonics* **2013**, *7*, 53–59.
- (41) Konstantatos, G.; Levina, L.; Fischer, A.; Sargent, E. H. Engineering the Temporal Response of Photoconductive Photo-

detectors via Selective Introduction of Surface Trap States. *Nano Lett.* **2008**, *8*, 1446–1450.

- (42) Ruffieux, P.; Cai, J.; Plumb, N. C.; Patthey, L.; Prezzi, D.; Ferretti, A.; Molinari, E.; Feng, X.; Müllen, K.; Pignedoli, C. A.; Fasel, R. Electronic Structure of Atomically Precise Graphene Nanoribbons. *ACS Nano* **2012**, *6*, 6930–6935.
- (43) Jung, G. H.; Yoo, S.; Park, Q. H. Measuring the Optical Permittivity of Two-Dimensional Materials Without a Priori Knowledge of Electronic Transitions. *Nanophotonics* **2019**, *8*, 263–270.
- (44) Mukherjee, B.; Tseng, F.; Gunlycke, D.; Amara, K. K.; Eda, G.; Simsek, E. Complex Electrical Permittivity of the Monolayer Molybdenum Disulfide (MoS2) in Near UV and Visible. *Opt. Mater. Express* **2015**, *5*, 447–455.
- (45) Lloyd, D.; Liu, X.; Christopher, J. W.; Cantley, L.; Wadehra, A.; Kim, B. L.; Goldberg, B. B.; Swan, A. K.; Bunch, J. S. Band Gap Engineering with Ultralarge Biaxial Strains in Suspended Monolayer MoS<sub>2</sub>. *Nano Lett.* **2016**, *16*, 5836–5841.
- (46) He, K.; Poole, C.; Mak, K. F.; Shan, J. Experimental Demonstration of Continuous Electronic Structure Tuning via Strain in Atomically Thin  $MoS_2$ . Nano Lett. 2013, 13, 2931–2936.
- (47) Lee, H. S.; Min, S. W.; Chang, Y. G.; Park, M. K.; Nam, T.; Kim, H.; Kim, J. H.; Ryu, S.; Im, S. MoS<sub>2</sub> nanosheet phototransistors with thickness-modulated optical energy gap. *Nano Lett.* **2012**, *12*, 3695–3700.
- (48) Miura, K. The Science of Miura-Ori: A Review. *Origami* 2009, 4, 87–99.